

## REPORT DOCUMENTATION PAGE

Public reporting burden for this collection of information is estimated to average 1 hour per response, including the time for reviewing the data needed, and completing and reviewing this collection of information. Send comments regarding this burden estimate or any other aspect of this collection of information, including suggestions for reducing this burden to Washington Headquarters Services, Directorate for Information Operations and Reports, 1215 Jefferson Davis Highway, Suite 1204, Arlington, VA 22202-4302, and to the Office of Management and Budget, Paperwork Reduction Project (0704-0188), Washington, DC 20503

0247

<b>1. AGENCY USE ONLY (Leave blank)</b>		<b>2. REPORT DATE</b> 12 April 2004	<b>3. REPORT TYPE AND DATES COVERED</b> 15-Feb-2003 to 31-Dec-2003	
<b>4. TITLE AND SUBTITLE</b> Three-dimensional structure of turbulent scalar fields with applications in aeroptics			<b>5. FUNDING NUMBERS</b> F49620-03-1-0102	
<b>6. AUTHOR(S)</b> Paul E. Dimotakis Christopher Martin				
<b>7. PERFORMING ORGANIZATION NAME(S) AND ADDRESS(ES)</b> California Institute of Technology 1200 E California Blvd. Pasadena, CA 91125			<b>8. PERFORMING ORGANIZATION REPORT NUMBER</b>	
<b>9. SPONSORING / MONITORING AGENCY NAME(S) AND ADDRESS(ES)</b> AFOSR 4015 Wilson Blvd., Room 713 Arlington, VA 22203-1954			<b>10. SPONSORING / MONITORING AGENCY REPORT NUMBER</b>	
<b>11. SUPPLEMENTARY NOTES</b>				
<b>12a. DISTRIBUTION / AVAILABILITY STATEMENT</b> Approved for public release; distribution is unlimited				<b>12b. DISTRIBUTION CODE</b>
<b>13. ABSTRACT (Maximum 200 Words)</b> This is the final report for AFOSR Grant F49620-03-1-0102, which ended 31 Dec 2003. This program aimed to develop an interferometric technique for mitigating the effects of turbulence on visible-light imaging, complementary to techniques such as Adaptive Optics (AO) or speckle imaging. This technique employs a rotation shearing interferometer and high-speed, low-noise digital imaging system. Where an AO system would employ a complex high-bandwidth electro-mechanical system to mitigate the effects of turbulence, this interferometric technique relies on a novel (low-cost) optical design, high-speed detector electronics, and digital post-processing to obtain images. One significant advantage of this technique is the use of a large-format detector, which enables correction of aberrating fields with power at far higher wavenumbers than AO systems can accommodate. Efforts have continued to analytically characterize the performance and limitations of this technique, and to analyze previously obtained astronomical data. Internal alignment algorithms have been automated to improve real-time performance. The read noise of the existing digital imaging system has been reduced, and its mechanical interface has been improved. Work has begun on a next-generation hybrid CMOS-CCD imaging system.				
<b>14. SUBJECT TERMS</b>			<b>15. NUMBER OF PAGES</b> 18	
			<b>16. PRICE CODE</b>	
<b>17. SECURITY CLASSIFICATION OF REPORT</b> Unclassified	<b>18. SECURITY CLASSIFICATION OF THIS PAGE</b> Unclassified	<b>19. SECURITY CLASSIFICATION OF ABSTRACT</b> Unclassified	<b>20. LIMITATION OF ABSTRACT</b> UL	

20040520 041

**GRADUATE AERONAUTICAL LABORATORIES**  
**CALIFORNIA INSTITUTE of TECHNOLOGY**  
Pasadena, California 91125

**Three-dimensional structure of turbulent scalar  
fields with applications in aeroptics**

Paul E. Dimotakis\* and Christopher Martin\*\*

Air Force Office of Scientific Research  
Grant No. F49620-03-1-0102

Final Scientific Report  
15 February 2003 through 31 December 2003

12 April 2004

**DISTRIBUTION STATEMENT A**  
Approved for Public Release  
Distribution Unlimited

---

\* John K. Northrop Professor of Aeronautics and Professor of Applied Physics  
\*\* Professor of Physics

## Summary

This research effort comprised the ongoing analysis and development of a novel interferometric technique for imaging through turbulence, as well as improvements to a high-speed, low-noise imaging system, as required for imaging through turbulence. There were two primary thrusts to this effort:

- Analysis and development of the Quadrature Phase Interferometer (QPI)
- Development of high-speed, low-noise digital imaging systems

Work on the QPI can be categorized into analytic, observational, and instrumentation efforts. The analytic efforts concern fundamental limitations on QPI performance, regarding maximum aberrating wavenumbers and reconstructed image characteristics. The observational efforts concentrate on analysis of data obtained at the Hale 200" Telescope at Palomar Observatory, observing both single (unresolved) and binary bright stars. A simple image reconstruction of a single star gives a reduction of the turbulence-limited image full-width half-max (FWHM) from 1 arcsec (in direct images) to 0.22 arcsec (relative to a 0.028 arcsec diffraction limit). Fitting a model to the binary star observations gives a binary separation (in two dimensions) that agrees with the expected positions with an accuracy 20× finer than the (unaberrated) diffraction limit of the telescope. Further improvements in the design and operation of the interferometer are underway, intended to internally align the interferometer in an automated fashion, thereby satisfying the most troubling performance constraint of the QPI. A paper describing the design, principles of operation, observations and analysis of the QPI technique is in preparation for submission to Applied Optics.

Development and testing of the Kilo-Frame per Second (KFS) high-speed, low-noise CCD camera has provided the best noise performance at high frame rates over a large format ( $1024 \times 1024$  pixel) camera to date, measuring under 26 e<sup>-</sup>/pixel rms noise for a 5 ms full-frame, unbinned readout and 15.5 e<sup>-</sup>/pixel for a 10 ms, full-frame, 2×2 binned readout time. The design and fabrication of a next-generation low-noise system, a Hybrid Imaging Technology 1 (HIT1) CCD, has progressed during this period, but has not yet yielded a working device. The HIT1 technology should enable a further reduction in read noise by a factor of 2-3, for comparable read times.

## Introduction

Several techniques have been developed to image through turbulence, including Adaptive Optics (AO), speckle interferometry, and non-redundant masking interferometry. The development of the QPI technique, which uses a rotation-shearing interferometer, complements these alternative imaging programs. The QPI has some advantages over other imaging techniques, under a number of observing conditions. The QPI has the potential to construct images in the presence of aberrating fields containing power at high spatial wavenumbers. The wavefront resolution of the QPI is up to 20 times that of contemporary AO systems. As presently implemented, QPI has 512 pixels spanning the input pupil, compared to ~ 30 actuators across the pupil in AO systems. The QPI is unaffected, to first order, by wavefront scintillation, which arises under conditions of strong turbulence, or long propagation distances through turbulence, or when observing

at short wavelengths. Such scintillation, if uncorrected, degrades imaging performance, even if phase aberrations across the wavefront are removed. The external calibration requirements of QPI are less stringent than that of other passive image reconstruction techniques (e.g., speckle interferometry), provided that the internal alignment of the interferometer is accurate.

The principles behind the QPI imaging technique are described in detail in Kern *et al.* (2001) and Kern *et al.* (2003). The QPI is a 180-degree rotation shearing pupil-plane interferometer, in a Mach-Zender arrangement. The instrument interferes two copies of the input pupil, rotated by 180 degrees with respect to one another. This is shown schematically in Fig. 1. The Mach-Zender arrangement allows for complementary interferograms to be recorded simultaneously, each of which shows the interference between the same two copies of the input pupil, but with 180° of interferometric phase difference between corresponding points in the two interferograms. Where one interferogram is bright, the other is dark.

The choice of a 180-degree rotation shear introduces a redundancy in the information content of the interferograms, which is exploited by introducing an instrumental phase shift in half of each interferogram. For each point in the interferograms, this instrumental phase offset allows four measurements to be made simultaneously (see Fig. 1 for examples), with four different instrumental phase (path length difference) contributions. This simultaneous measurement of four intensities allows for an instantaneous

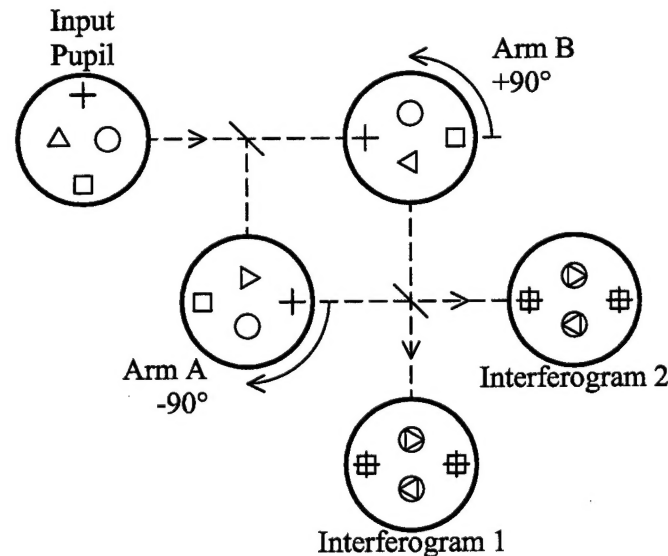


Fig. 1. Schematic representation of rotation-shearing interferometer operation. Four points in the input pupil are shown, which pass through a beamsplitter into the two arms of the interferometer, then through a second beamsplitter to recombine into two interferograms. The superposition of points from opposite sides of the input pupil causes the intensity in the interferograms to be modulated by the visibility function of the object under study. Each interference pair (e.g., cross and square, or circle and triangle) appears in two places in each of the two output interferograms, allowing four measurements for each interference pair.

determination of the full complex visibility, as well as a map of the wavefront amplitude across the pupil. The complex visibility is the fundamental measurement made by the interferometer. It is convenient to discuss the modulus and phase of the complex visibility separately, as  $\gamma(u,v) = V(u,v) \exp\{i\phi(u,v)\}$ , where  $u$  and  $v$  denote the location in the interferograms (equivalent to angular wavenumbers). The Fourier Transform of the complex visibility (sampled in two dimensions) is the reconstructed image. Phase aberrations in the input wavefront affect the measured visibility phase,  $\phi(u,v)$ , but not the measured visibility modulus,  $V(u,v)$ . The phase aberrations can be eliminated from the complex visibility by an averaging technique (circular averaging of the phase gradients).

Interferograms measured by the QPI have intensities modulated by turbulent aberrations, which may have characteristic timescales of tens of milliseconds, or less. For timescales this short, the important performance issues are signal-to-noise ratio of the measurements and exposure duty cycle. Low detector noise emerges as an important attribute because short exposures do not permit the collection of large amounts of light. Short readout times are desirable both to maximize the net exposure in a given period of time, and to permit the formation of a contiguous time-series of observations to track turbulent aberrations.

The KFS digital-imaging system uses a custom-built (1024×1024)-pixel CCD, optimized to deliver low read noise (under 30 e<sup>-</sup>/pixel rms) for full-frame read times as short as 5 ms. It was developed under DURIP Grant F49620-95-1-0199, and AFOSR Grants F49620-98-1-0052, F49620-01-1-0006, and F49620-00-1-0036, and provides the best solution for the imaging demands of the QPI. It is described in detail in Kern *et al.* (2001). A next-generation imaging system, the Hybrid Imaging Technology 1 (HIT1) CCD, with an expected read noise reduction by a factor of 2-3 relative to the existing KFS system, has been fabricated but is not operational. The HIT1-CCD development was also funded by AFOSR Grant F49620-01-1-0006.

## **QPI Analytic Efforts**

Two aspects of the QPI technique were examined in detail using analytic studies. First, the relationship between the number of detector pixels and the maximum wavenumber of turbulent phase aberrations that can be compensated was determined using an assumption of Kolmogorov turbulence. Second, the Point-Spread Function (PSF), and therefore the Modulation Transfer Function (MTF), of the QPI technique were examined, to explain differences in images reconstructed using the QPI and direct images.

### **QPI Analytic Efforts: Maximum Aberrating Wavenumber**

By the nature of the interferometric observations, all phase measurements are wrapped, *i.e.*, only the true phase modulo  $2\pi$  is known. It is then convenient to use directional statistics when describing and analyzing phase measurements. For example, circular averaging is a technique used to find the mean direction, which is defined as

$$\theta^{av} = \text{atan} \left( \frac{\sum_i \sin \theta_i}{\sum_i \cos \theta_i} \right), \quad (1)$$

(Mardia 1972) for a set of phases (or, generally speaking, directions)  $\theta_i$ .

The subsequent statistical analysis of phases depends on the assumed statistical properties of the turbulent phase. It is common to assume that the turbulence is isotropic and homogeneous, which leads to a description of the fluctuations in the Optical Path Length (OPL) at the input pupil in terms of a structure function (Fried 1965). This structure function,  $D_l(r)$ , can be defined by

$$D_l(r) = \langle [l(\vec{x}) - l(\vec{x} + \vec{r})]^2 \rangle, \quad (2)$$

where the angular brackets denote an expectation,  $l$  is a variation in OPL, and  $r$  is the magnitude of the vector  $\vec{r}$ . The orientation of the vectors  $\vec{x}$  and  $\vec{r}$ , located in the input pupil, do not affect  $D_l(r)$ . The additional assumption commonly made is that the fluctuations in  $l$  are normally distributed. Under these assumptions (isotropic, homogeneous, normally distributed OPL fluctuations), the distribution of wrapped turbulent phase terms is a wrapped normal distribution with zero mean.

The goal of any phase retrieval technique is to remove the turbulent phase terms. Because the turbulent phase terms have zero mean, one approach would be to simply average the measured phase terms, using Eq. 1, to remove the turbulent phase terms. However, when the variance of the linear turbulent phase terms is more than a radian<sup>2</sup>, the distribution of the sample mean direction of the phases is very broad. If  $\theta_i$  is distributed normally with variance  $\sigma^2$  and mean 0, the asymptotic distribution of the mean direction  $\theta^{av}$ , for a large number of independent samples,  $n$ , has a variance given by

$$\langle (\theta^{av})^2 \rangle = \frac{\exp(\sigma^2) - \exp(-\sigma^2)}{2n} \quad (3)$$

(Mardia 1972).

The number of samples required for a given level of accuracy in the sample mean scales exponentially with the underlying variance. Under imaging conditions of interest (where direct imaging is insufficient), the variance of the turbulent phase terms may be many hundreds of radians<sup>2</sup>, making this technique entirely ineffective.

The approach to circular averaging taken in this investigation is to average the phase gradients rather than the phase itself. If  $l(x,y)$  is the OPL as a function of position in the input pupil, with  $(x,y) = (0,0)$  corresponding to the center of the input pupil, then the turbulent phase corresponding to pairs of points that interfere is  $\phi_{turb}(x,y) = [l(x,y) - l(-x,-y)] 2\pi/\lambda$ . The variance of  $\phi_{turb}(x,y)$  is  $D_\phi(2r) = (2\pi/\lambda)^2 D_l(2r)$ , where  $r^2 = x^2 + y^2$ . Defining the gradients by finite differencing,

$$\nabla_x \phi = \phi(x + \Delta x, y) - \phi(x, y), \quad (4)$$

they are useful when rewritten as



$$\begin{aligned}\nabla_x \phi \lambda / 2\pi &= [l(x+\Delta x, y) - l(-x-\Delta x, -y)] - [l(x, y) - l(-x, -y)] \\ &= [l(x+\Delta x, y) - l(x, y)] + [l(-x, -y) - l(-x-\Delta x, -y)].\end{aligned}\quad (5)$$

These gradients have a variance given by

$$\frac{\langle (\nabla_x \phi)^2 \rangle}{(2\pi / \lambda)^2} = 2D_l(\Delta x) + 2 \left\langle \frac{[l(x+\Delta x, y) - l(x, y)] \cdot [l(-x, -y) - l(-x-\Delta x, -y)]}{[l(x+\Delta x, y) - l(x, y)] + [l(-x, -y) - l(-x-\Delta x, -y)]} \right\rangle. \quad (6)$$

The same relationships exist for the  $y$ -gradients. The relative magnitudes of the terms on the right-hand sides of the variance expressions depend on the form of the structure function,  $D_l$  (or  $D_\phi$ ). Taking Kolmogorov turbulence as an example<sup>13</sup>,

$$D_\phi(r) = 6.88 (r/r_0)^{5/3} \text{ rad}^2, \quad (7)$$

where  $r_0$  is Fried's coherence length, when  $\Delta x \ll \sqrt{x^2 + y^2}$  the cross-term in Eq. 13 will be much smaller than  $D_l(\Delta x)$ . The same argument holds for  $\Delta y$ . The approximation used for this analysis is that, for  $\Delta x = \Delta y$ ,

$$\langle (\nabla_x \phi)^2 \rangle = \langle (\nabla_y \phi)^2 \rangle \approx 2D_\phi(\Delta x). \quad (8)$$

The most important implication of Eq. 15 is that the variance of the sample mean direction of each gradient,  $\nabla_x^{\text{av}} \phi$  and  $\nabla_y^{\text{av}} \phi$ , will be given by Eq. 3, with  $\sigma^2 = 2D_\phi(\Delta x)$ . For small  $\sigma^2$ , Eq. 3 reduces to the familiar result from the linear (unwrapped) normal distribution, with a variance of the sample mean given by  $\sigma^2/n$ . However, in order to ensure that the positive exponential term does not dominate, an approximate limit is

$$2D_\phi(\Delta x) < 1 \text{ rad}^2. \quad (9)$$

The use of this technique, which is the only practical way to retrieve phase information under ordinary imaging scenarios, imposes a limit on the pixel spacing,  $\Delta x$ , as a function of  $r_0$ . Combining Eqs. 7 and 9, we get approximately

$$\Delta x < r_0/5. \quad (10)$$

For a given aperture diameter and number of pixels, this limits the turbulent conditions under which meaningful phase measurements may be made, or alternately, for a given number of pixels and turbulent conditions, this limits the aperture diameter which may be used.

As an example, for an 18" aperture spanned by 512 pixels, the minimum  $r_0$  that can be accommodated is approximately 4 mm. As another example, with  $r_0 = 10$  cm and a 200" aperture (astronomical observing), at least 250 pixels across the input pupil are required.

### **QPI Analytic Efforts: Imaging Considerations**

There is a fundamental difference in the imaging performance of direct imaging systems and interferometric imaging systems, in the absence of aberrations. Given a circular input pupil, the Point-Spread Function (PSF) of a direct imaging system (with no aberrations) is the square of an Airy function, while the PSF of an interferometric imaging system is an Airy function (which is not squared).

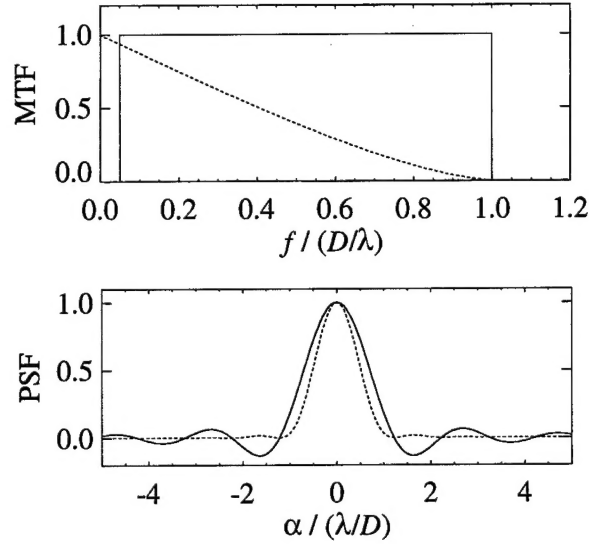


Fig. 2. Unaberrated MTF and PSF of direct and QPI images. Solid lines are the QPI functions, dashed lines are direct images. The pupil diameter is  $D$ , the wavelength of observation is  $\lambda$ ,  $\alpha$  measures angular position in the images, and  $f$  is angular frequency.

Another interpretation of the difference between the PSFs of direct and interferometric imaging is that the Modulation Transfer Functions (MTFs) differ. The MTF is the modulus of the Fourier Transform of the PSF (Born & Wolf 1999), and represents the transfer function of objects with sinusoidal intensities, as a function of sinusoidal frequency. The MTF of a direct imaging system decreases out to the cutoff frequency of  $D/\lambda$ , where  $D$  is the pupil diameter and  $\lambda$  is the wavelength of observation. The MTF of the QPI is constant over all frequencies, up to the cutoff frequency. The PSF and MTF of direct and QPI systems are all shown in Fig. 2.

An important aspect of the QPI is that the MTF is zero for zero angular frequency. This is due to a small split between the mirrors that create the quadrature phase relationship in the interferometer. The absence of low-frequency information, shown also in the MTF plot of Fig. 2, leads to a high-pass filtering effect on the interferometric images. Fig. 3 shows direct and interferometric images of the same scene, which shows clearly that the QPI is well adapted to detecting sharp features (high frequencies) in images, but does not transmit slowly varying intensities (low frequencies) well. This is also evident in the MTF and PSF plots of Fig. 2.

## QPI Observational Effort

The QPI observed a handful of astronomical objects at the coudé focus of the Hale 200" Telescope at Palomar Observatory, in July 2002. Data obtained on Vega, a bright unresolved star (effectively a point-source) and Capella, a close binary system, were analyzed to demonstrate the imaging capabilities of the QPI technique.



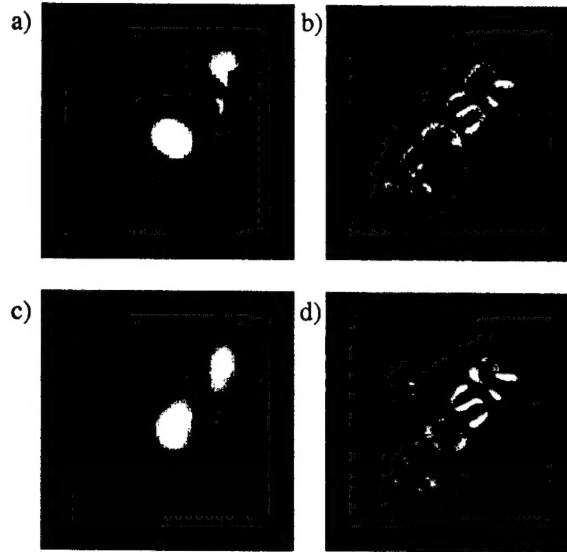


Fig. 3. Direct and interferometric laboratory images, without and with aberrations. The left-hand panels (a and c) are direct images, the right-hand panels (b and d) are interferometric images. The top two panels (a and b) have no turbulent aberrations, the bottom two (c and d) have aberrations introduced using a turbulent He jet. The aberrated direct image (c) is unrecognizable, while the aberrated interferometric image (d) is nearly unaffected. (b) and (d) show sharp features well, but lose low-frequency information.

#### **QPI Observational Effort: Vega**

Vega was observed over a 40 nm bandpass at a mean wavelength of 700 nm, with 12.5 ms exposures followed by a 12.5 ms readout, for a frame rate of 40 Hz. During readout, pixels were binned in a 2×2 pattern, reducing the number of effective pixels on the KFS to 512×512 pixels, which gives 256 pixels across each interferogram. Data was acquired for 10 s (400 frames) before data acquisition stopped, and the data was transferred to disk. A sample interferogram is shown in Fig. 4.

The complex visibility was extracted from the interferograms in each frame, as described in Kern *et al.* (2001) and Kern *et al.* (2003), after self-calibrating the instrumental phase offsets. Visibility phase gradients were constructed and circularly averaged over all

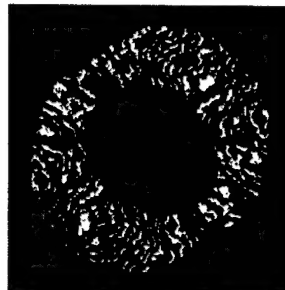


Fig. 4. Sample interferogram of Vega. The visibility modulus (fringe contrast) is uniformly high across the interferogram. The thin horizontal gap through the center of the interferogram is the separation between upper and lower quadrants of the interferogram.

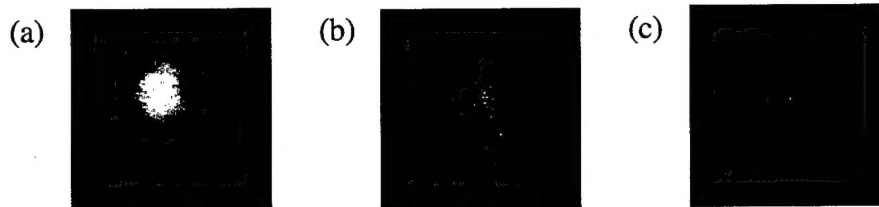


Fig. 5. (a) Direct, (b) raw interferometric, and (c) differenced interferometric images of Vega, all taken from 400 frames (10 s) of data. The raw interferometric image contains undesired instrumental visibility phase terms. The visibility phase of the differenced image is the difference between the phase from the first 5 s and the second 5 s of data, and is a measure of the phase noise. The FWHM of the images are (a) 1 arcsec, (b) 0.5 arcsec, and (c) 0.2 arcsec.

frames, then the average gradients were used to reconstruct the mean visibility phase. The reconstructed image is then the Fourier Transform of the mean complex visibility, as defined by the mean visibility modulus and the mean visibility phase. This reconstructed image includes instrumental phase terms (as distinct from the instrumental phase offsets, which are differences between instrumental phase terms in different quadrants). The absolute value of the reconstructed image is shown in Fig. 5, which is representative of the width of the PSF. The direct image, obtained simultaneously, is also shown in Fig. 5 for comparison.

From a single 10 s dataset, the instrumental phase terms can be removed by differencing the mean visibility phase determined from the first 5 s with the mean visibility phase determined from the second 5 s. This differenced visibility phase contains no instrumental phase term, but also contains no object visibility phase terms, and contains twice the measurement noise of the full 10 s mean visibility phase. The reconstructed image formed using the differenced visibility phase serves as a raw measure of the noise of the imaging process. The absolute value of the image formed from the differenced visibility phase is also shown in Fig. 5.

The full width half-max (FWHM) of the direct image is 1 arcsec, the FWHM of the image formed from the mean visibility phase is 0.5 arcsec, and the FWHM of the image formed from the differenced visibility phase is 0.2 arcsec.

The complex visibilities associated with these images show some calibration errors. Further analysis is expected to remove these errors, which will improve the imaging quality further. The current performance is still significantly poorer than the diffraction-limited resolution, which would have a FWHM of 0.028 arcsec.

### **QPI Observational Effort: Capella**

Capella is a binary star system, comprising two stars of nearly equal brightness in a 100-day orbit. The semi-major axis of the binary orbit is approximately 0.050 arcsec, which is unresolved under ordinary seeing conditions ( $\sim 1$  arcsec), but larger than the diffraction limit of the Palomar 200" telescope (0.028 arcsec at 700 nm).

Capella was observed using the same configuration as Vega, described above. However, when Capella was observed, the interferometer alignment was incorrect, and the rotation shear was not 180 degrees. With a rotation shear sufficiently different from 180 degrees,

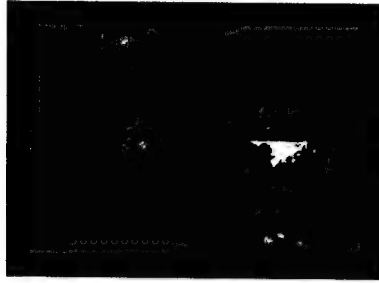


Fig. 6. Visibility modulus of Capella. The coudé flat vignettted the pupil, removing light from the top-right and bottom-left regions of the image. The pupil was then displaced from the QPI center of rotation to maximize the interfered area. The visibility modulus (no visibility phase information was available) shows the sinusoidal modulation of a binary star (the Fourier Transform of two delta-functions is a sine function).

there is no quadrature relationship between points in the interferogram quadrants. Therefore, visibility modulus measurements may be extracted from the Capella observations, but visibility phase measurements are unavailable. In addition, there was significant vignetting due to the coudé flat mirror. As a result of the vignetting, the center of the input pupil was intentionally displaced from the center of rotation of the interferometer, to maximize the area in the interferograms that shows interference. The net effect was that the interferograms were not at all circular, and the area showing interference was much less than it would have been without the vignetting.

Capella's visibility modulus is shown in Fig. 6. The visibility modulus was computed by differencing the two interferograms (which are guaranteed to differ by  $180^\circ$  in visibility phase), but without requiring any calibration (not even dark subtraction and flat-fielding of the CCD images). The modulus shows a sinusoidal pattern, which is the signature of a binary system (the Fourier Transform of two delta-functions is a sine function). The sinusoidal frequency determines the magnitude of the binary separation, and the orientation of the sinusoidal pattern determines the orientation of the binary separation. By fitting a simple sinusoid to the observed visibility modulus, a binary separation of 0.055 arcsec at a position angle of 21 or 201 degrees (E of N) is obtained. When using only the visibility modulus, position angles are inherently insensitive to 180-degree rotations.

The orbit of Capella has been determined by other interferometric measurements, and is described in Hummel et al. (1994). A plot of the orbit of Capella, as determined by Hummel et al. (1994), is shown in Fig. 7, with the position determined by the QPI measurements overlaid. Excluding the measurement that is 180 degrees away from the expected position, the disagreement between the expected and measured binary separation is only 0.0012 arcsec. This is significantly better than the diffraction limit of the telescope, which is 0.028 arcsec. This super-resolution can be attributed in part to the fact that the visibility modulus is measured at a large number (9,000) of independent points (*i.e.*, pixels), despite the fact that the vignetting resulted in a great reduction in the number of points at which interference is visible.

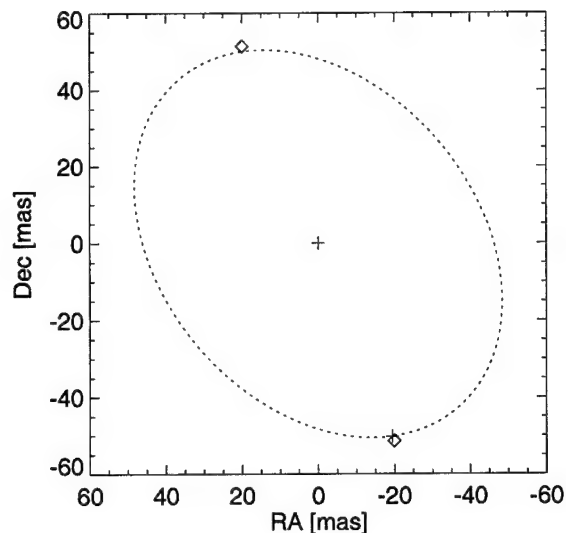


Fig. 7. Capella's binary separation. One star is assumed to be at the origin (the center cross), the relative position of the second traces out the dotted line. The expected separation at the time of the QPI measurements is given by the cross in the lower-right, the measured separation is given by the diamonds. There are two diamonds because modulus-only measurements are uncertain to 180 degrees. The difference between expected and measured separations is 0.0012 arcsec.

### QPI Instrumentation Effort

There are several alignment requirements that the QPI must adhere to. The most stringent, in a linear sense, are the optical path length alignments, which should give zero phase (*i.e.*, path length) difference through the interferometer for one quadrant and 90° through the other. On-axis rays that pass through the two arms of the interferometer should remain parallel at the output. Less stringent requirements are placed on the lateral displacement of wavefronts, which is equivalent to a shift of the QPI center of rotation. The final restriction is on the rotation shear introduced by the QPI, which should be  $180 \pm 0.5$  degrees.

When interfacing the QPI with a telescope, whether a large aperture such as the Palomar 200" telescope or an 18" telescope for field tests, the position and tilt of the telescope pupil, as seen by the QPI, must also be adjusted. When taking data at Palomar, the degrees of freedom necessary to allow independent position and tilt of the input pupil were not all available, which necessitated realignment of the interferometer for each new target. This problematic solution resulted in improper alignment, with an incorrect rotation shear during the Capella measurements (eliminating the possibility of quadrature phase measurements), and loss of interference in the case of Vega (note the noncircular boundaries, and the oddly-shaped, overly large obscuration in Fig. 4).

The camera control software and the interferometer alignment software have been modified to communicate with each other, and closed-loop control algorithms have been implemented to allow a rapid, mostly automated alignment sequence. The goal has been to execute a full alignment sequence in under one minute, which has not yet been

realized, as some steps in the process still require manual input. The alignment process does, at present, always converge on a satisfactory alignment.

## Digital Imaging

The digital-imaging and high-speed data-acquisition part of this effort has mostly focused on hardware development, with software/firmware developments on an as-necessary basis. The data acquisition subsystem was developed by Daniel Lang with assistance from Garrett Katzenstein, Brian Kern, Steve Kaye, and supervised by Paul Dimotakis. This part of the effort was cofunded by DURIP Grant F49620-95-1-0199, and AFOSR Grants F49620-98-1-0052, F49620-01-1-0006, and F49620-00-1-0036.

### KFS Camera Data-Acquisition System

The KFS camera system is a camera system designed for high-speed low-noise image acquisition. The KFS camera CCD image sensor was designed by Mark Wadsworth of JPL. It has a resolution of  $1024 \times 1024$  pixels, with 32 output channels, to acquire up to 1000 images per second. The KFS camera head electronics were designed by Daniel Lang with assistance from Steve Kaye. The original camera head housing was designed by Pavel Svitek. The KFS camera system includes a VXI bus enclosure with 8 4-channel A/D converter boards (VXIADC2), for a total of 32 channels, a VXI timing board (VXITIM2), a VXI power board (VXICAM2), and a control PC (Fig. 8).

At this time, the KFS CCD image sensor and data acquisition system relies on a  $1024 \times 1024$  CCD with 32 output channels at 40 MHz, for up to 1000 fps (frames/second). The system has been tested to 333 fps (current lasers limit us to 200 fps). 8 VXIADC2 boards are operating, with 4 12-bit A/D converters and 512 MB memory for 4 GB total memory. The system can acquire 2700 contiguous frames (12-bit packed), or 4000 to 8000 contiguous frames with lossless compression. An auxiliary data port is provided on each A/D board for future disk-storage and faster data-acquisition expansions.

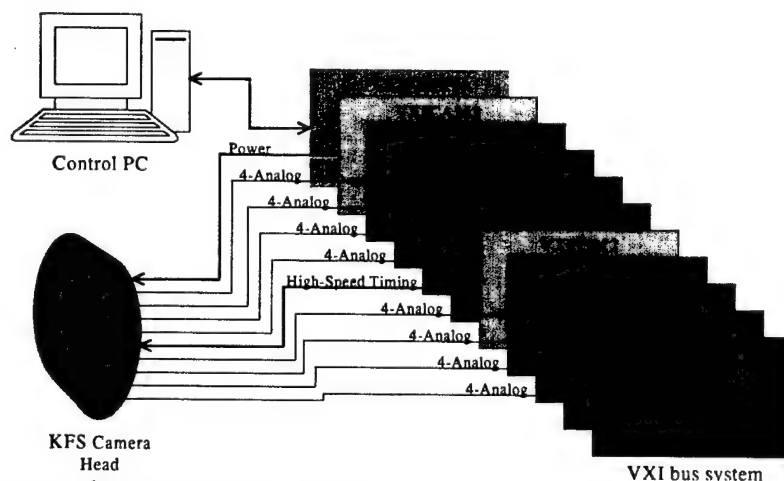


Fig. 8. KFS camera data acquisition system.

## KFS Camera Data-Acquisition System

The KFS data-acquisition system has been completed and is working well. Low-light level applications, however, as encountered in its use in gas-phase imaging or at the Palomar observatory, can benefit from improved noise figures. The plot below shows the original noise figures (1024×1024) and original binned noise figures (binned to 512×512) in electrons/pixel.

A new VXI enclosure was installed with a separate low-noise power supply for the analog circuits. Also, the analog inputs on the VXI A/D converter boards were adjusted to maximize the Common Mode Rejection Ratio (CMRR). The resulting improved noise figures are shown on the "New Chassis" and "New Ch. Binned" graphs in Fig. 9.

Finally, the CCD camera was connected to a liquid nitrogen dewar and the assembly was evacuated. The liquid nitrogen cools the CCD using a cold finger designed by Brian Kern for operational temperature down to -38° C. The final improved noise figures are shown on the "CCD Cooled" and "Cooled Binned" graphs in Fig. 9.

### New KFS/HIT1 Camera Head Design

A problem encountered with evacuating the camera and cooling the CCD is that vacuum grease and heat sink grease evaporates from the warmer surfaces and condenses on the coldest item, the CCD image sensor itself. Another problem is that the shutter deposits small dust particles on the surface of the CCD. This has led to a redesign of the camera head to minimize these problems and simplify manufacture of the camera head. The new design places the shutter in front of the optical window and the power board at the rear of the camera leaving only the CCD board inside the evacuated enclosure. The new design reduces the number of hermetic connectors from 34 to 4 (the 32 coaxial video connectors are replaced by two 50-pin connectors), reducing the chances of leaks, eliminating custom cables, and simplifying assembly. The new camera head also provides additional voltages for the HIT1-CCD hybrid image sensor. Daniel Lang designed the PC boards and Garrett Katzenstein designed the enclosure for the new camera head. The new

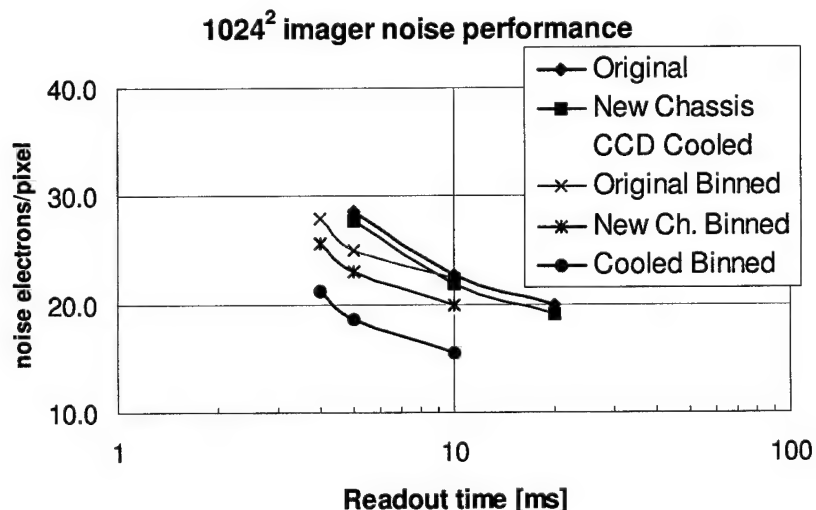


Fig. 9. KFS camera noise performance.

camera head has been assembled and tested and is working with the KFS CCD image sensor.

### HIT1-CCD Image Sensor

In the summer of 2003, ImagerLabs delivered the first prototypes of Hybrid Imaging Technology 1 (HIT1)-CCD sensors to Caltech. The novel sensor uses the photon conversion strengths of Charge Coupled Devices (CCDs) to achieve high fill factor (FF) and high Quantum Efficiency (QE), along with the advantages of CMOS for high speed, low noise signal processing to read images from the chip. The noise vs. frame rate design specifications comparing the HIT1-CCD to the KFS CCD are shown in the table below.

Parameter	KFS CCD	HIT1-CCD	Units
CCD output taps	32	256	-
Output Ports	32	32	-
Noise @ 50 fps	17	<5	Electrons rms
Noise @ 100 fps	20	<6	Electrons rms
Noise @ 200 fps	26	<10	Electrons rms

HIT1 technology relies on an 8-fold increase in the number of output channels (to 256) at the CCD-to-CMOS interface to decrease readout bandwidth of each channel, for a given frame (pixel) rate. A HIT1-CCD is shown in Fig. 10.

Mark Wadsworth designed the CCD image sensor and Gene Atlas of ImagerLabs designed the CMOS processors. Two CMOS processors are bump-bonded to two ends of the HIT1-CCD chip using Indium balls. Each CMOS processor provides amplification, filtering and Correlated Double Sampling (CDS) for 128 input channels. The 128 processed signals are multiplexed down to 16 output channels. The 32 processed channels (16 on each end) are fed out of the HIT1-CCD image sensor package and then processed by the present 32 channel A/D converter system. The CMOS processors have selectable input filters optimized for 30 and 200 fps.

The devices received were not functional. ImagerLabs separated the HIT1 devices to discover that the CMOS-CCD interconnects were shorted to one another. The problem was tracked with the hybrid service vendor, where an incorrect tool was used for the

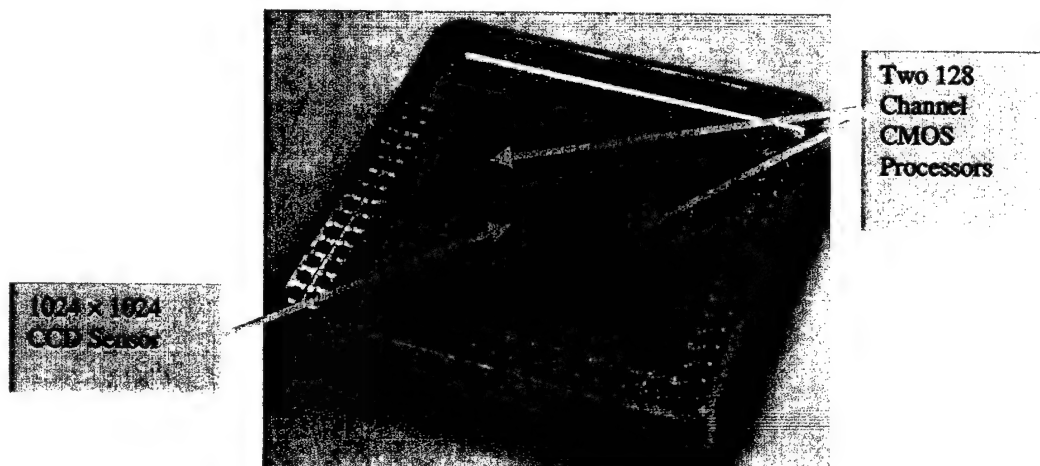


Fig. 10. HIT1-CCD image sensor.



interconnect (the interconnects were larger than specified).

The following describes work completed since the end of this grant, or work presently in progress, and is included below to bring the present status report up to date.

Date	Milestone	Costs
Feb. 18	Fully operational bonder and hybridization tools	
Mar. 8	1 <sup>st</sup> successful Single channel HIT device	7 scrapped single channel CMOS processors
Mar. 19	3 successive perfect single channel HIT devices	0 defects
Mar. 26	1 <sup>st</sup> successful 8 channel CMOS processor	10 scrapped 8-channel CMOS processors

To gain control of the critical hybridization step, ImagerLabs has developed the process technique in-house. ImagerLabs has acquired all the necessary equipment and tooling for interconnect deposition, alignment and hybridization of the devices.

The difficulties of bond placements on long devices have been surmounted, and correction algorithms for optical angular misalignments have been developed. Sample images of the bond pads are shown in Fig. 11. This progress was achieved using cheaper and more readily available single channel and small multi-channel CMOS processors and CCDs from ImagerLabs' stock of devices, reserving the more valuable KFS 1K wide CMOS processors and large CCDs.

Hybridization attempts on the Caltech HIT1-CCD sensors are in preparation. The chance of constructing an unshorted HIT1 device is estimated to be greater than 75% on the first attempt. There is enough material on hand to deliver an additional 4 devices. The probability of constructing 2 unshorted HIT1 devices is estimated to be greater than 95%.



### Old Bonds and Samples from new tool, 175um pad pitch



Top View - No  
Shorts

Pads

Balls



Top View Shorts

Fig. 11. Images of CMOS-CCD bond pads.

## High-speed Disk Array

The current KFS data acquisition system has 4 GB of high-speed memory, as discussed above. For most applications, this is sufficient for imaging in two dimensions, as a function of time, at low to moderate frame rates. For imaging 3-dimensional voxels, or for long-duration recording, the data requirements increase by a factor of 20 to 100, exceeding the memory capacity of the current data-acquisition system. Jan Lindheim of CACR has developed a Datawulf storage array as part of our NSF-funded TeraVoxel project. Each Datawulf storage array is based on a high-end PC with 64-bit PCI slots, 2 Raid disk controllers, 14 low cost Ultra-ATA disk drives of 250 GB each, and a Gigabit Ethernet interface, for a storage capacity of 3 TB per array, for a total of 24 TB.

At this writing, an S-Link interface between the A/D converter boards and the Datawulf storage arrays is under development. The S-Link (Simple Link) was developed by CERN and provides a low-overhead high-speed (128 MB/s) fiber-optic data pipe from a source node to a destination node. Eight S-Links provides a maximum aggregate transfer rate of 1 gigabyte per second which is sufficient to allow 800 to 1000 frames/second when data compression is enabled. The eight Datawulf storage arrays provide a total of 24 terabytes of storage, allowing us to increase the maximum run time by a factor of 6000.

The following S-Link boards have been purchased (10 each):

- CT-ODIN-3LSC1 S-Link Source Card (128MB/s, 1 fiber pair),
- CT-ODIN-3LDC1 S-Link Destination Card (128MB/s, 1 fiber pair), and,
- S32PCI64 S-Link to 64-bit PCI adapter card.

Each S-Link destination card plugs into a S32PCI64 adapter card, which then plugs a PCI slot on one of the Datawulf storage nodes. Each S-Link source card is mounted to a VXIADC2 A/D converter board using an ADC2SLINK adapter board designed by Daniel Lang. Currently, the software to read the data from the S-Link destination card and store it into the disk array is under development.

## Conclusions

The experiments undertaken during the period of effort have demonstrated some of the imaging performance of the QPI under real (astronomical) observing conditions, and have continued to evaluate the ultimate limitations to this technique. The KFS camera system has been optimized for low read noise at high frame rates, and development of a next-generation imaging system, with improvements in read noise by a factor of 2-3, has begun.

## Acknowledgements

The various components of this program were supported by a number of grants, listed below:

- DURIP Grant F49620-95-1-0199 supported the KFS CCD development
- NSF Grant AST9618811 supported the QPI and KFS CCD development
- AFOSR Grant F49620-98-1-0052 supported the KFS CCD development
- AFOSR Grant F49620-00-1-0036 supported QPI and KFS CCD development
- AFOSR Grant F49620-01-1-0006 supported KFS and HIT1 CCD development

## References Cited

- Born, M., Wolf, E. 1999, *Principles of optics* (New York: Cambridge University Press).
- Fried, D.L. 1966, "Optical Resolution Through a Randomly Inhomogeneous Medium for Very Long and Very Short Exposures," *Applied Optics* **56**, 1372-1379.
- Hummel, C.A., Armstrong, J.T., Quirrenbach, A., Buscher, D.F., Mozurkewich, D., Elias, N.M. II, Wilson, R.E. 1994, "Very high precision orbit of Capella by long baseline interferometry," *Astron. J.* **107**, 1859-1867.
- Kern, B., Lang, D.B., Martin, C., Dimotakis, P.E., Wadsworth, M. 2001, "A High-Speed Quadrature-Phase Rotation-Shearing Interferometer for Imaging Through Turbulence," *32<sup>nd</sup> AIAA Plasmadynamics and Lasers Conference*, AIAA 2001-2797.
- Kern, B., Dimotakis, P.E., Lang, D.B., Martin, C., Thessin, R.N. 2003, "Aberrating Medium Characterization and Image Reconstruction with a Quadrature-Phase Interferometer." *34<sup>th</sup> AIAA Plasmadynamics and Lasers Conference*, AIAA 2003-3610.
- Mardia, K.V. 1972, *Directional Statistics* (New York: Academic Press).

## Research Personnel Supported

- Dimotakis, Paul E., John K. Northrop Professor of Aeronautics and Professor of Applied Physics (PI)
- Katzenstein, Garrett, Research Engineer, Aeronautics
- Kaye, Stephen, Electrical Engineer, Physics
- Kern, Brian, Postdoctoral Fellow, Aeronautics
- Lang, Daniel B., Research Engineer, Aeronautics
- Martin, Christopher, Professor of Physics (Co-I)
- Mojahedi, Christina, Administrative Assistant, Aeronautics
- Thessin, Rachel, Undergraduate Student, Applied Physics

## **Collaborators**

- Atlas, Gene, President and CEO, Imager Labs (HIT1 design)
- Boyadzhyan, Victor, Research Engineer, Jet Propulsion Lab (KFS, HIT1 design / fab)
- Bredthauer, Richard, Research Engineer, Jet Propulsion Laboratory (KFS fab)
- Collins, Stuart Andrew (Andy), Research Engineer, Jet Propulsion Lab (KFS, HIT1 design / fab)
- Dingizian, Arsham, Research Engineer, Jet Propulsion Lab (KFS, HIT1 design/fab)
- Elliott, Stythe Thomas (Tom), Research Engineer, Jet Propulsion Lab (KFS, HIT1 design / fab)
- Kullman, Richard, Vice-President and Business Manager, Imager Labs (HIT1 design)
- Wadsworth, Mark W., Research Engineer, Jet Propulsion Lab (KFS, HIT1 design / fab)

## **Honors / Awards**

Honors, degrees, and awards received during period, as well as, "lifetime achievement honors such as Nobel prize, honorary doctorates, and society fellowships prior to this effort":

- Dimotakis, P.E.:
  - John K. Northrop Chair, Aeronautics, Caltech (February 1995)
  - Associate Fellow, AIAA (June 1989)
  - Fellow, Am. Phys. Society (November 1980)
- Martin, C.:
  - Uhl Prize for Outstanding Research in Astrophysics, U.C. Berkeley (1985)
- Kern, B.:
  - Michelson Postdoctoral Fellowship Award (July 2002)

## **Publications of work supported under this Grant**

Kern, B., Dimotakis, P.E., Lang, D.B., Martin, C., Thessin, R.N. 2003, "Aberrating Medium Characterization and Image Reconstruction with a Quadrature-Phase Interferometer." *34<sup>th</sup> AIAA Plasmadynamics and Lasers Conference*, AIAA 2003-3610.